Measurement of Dynamical Forces between Deformable Drops Using the Atomic Force Microscope. I. Theory

Steven L. Carnie,*,† Derek Y. C. Chan,† Craig Lewis,† Rogério Manica,† and Raymond R. Dagastine‡

Department of Mathematics and Statistics and Department of Chemical and Biomolecular Engineering, Particulate Fluids Processing Centre, The University of Melbourne, Parkville 3010, Australia

Recent experimental developments have enabled the measurement of dynamical forces between two moving liquid drops in solution using an atomic force microscope (AFM). The drop sizes, interfacial tension, and approach velocities used in the experiments are in a regime where surface forces, hydrodynamics, and drop deformation are all significant. A detailed theoretical model of the experimental setup which accounts for surface forces, hydrodynamic interactions, droplet deformation, and AFM cantilever deflection has been developed. In agreement with experimental observations, the calculated force curves show pseudo-constant compliance regions due to drop flattening, as well as attractive pull-off forces due mainly to hydrodynamic lubrication forces.

1. Introduction

The atomic force microscope (AFM) has long been used to make direct measurements of the forces acting between rigid particles of colloidal dimensions. Attention has since turned to the interaction between deformable surfaces, such as the interaction between rigid probe particles and oil drops[1−4] or between a particle and a bubble.[5] The hydrodynamic interaction of a rigid colloid probe with a solid surface[6,7] and with a liquid drop[8] has also been studied using the AFM.

Recently Dagastine et al.[9] made the first direct AFM measurements of the force between two approaching droplets of decane ($\approx$40 μm radius) in an aqueous solution of SDS. The observed forces show systematic variations with relative velocities in a range comparable to that due to thermal motion of such droplets in suspension.

In this paper, we model the AFM force measurement experiment between two drops in the experimental configuration of Dagastine et al.[9] In this experimental setup, one drop is attached to the AFM cantilever with known spring constant K. The other drop is attached to a piezoelectric stage that is moved according to a pro-grammed velocity schedule. For example, the stage is moved toward the cantilever with constant velocity V over a displacement X_{max} and is then reversed over the same

distance. That is, the piezo displacement follows a triangular sweep.

During the programmed velocity schedule, the deflection of the spring is recorded and converted to a force F using the spring constant of the cantilever. Therefore, the experimental data consist of pairs of values (X_i, F_i), the piezoelectric stage position and the corresponding force. Note that the separation between the piezoelectric stage and the cantilever, much less the minimum separation between the drops, is unknown, even initially. Hence, there is the need to relate experimental data to a force−separation law.

A characteristic feature seen in the measured forces between decane drops[9] is the dependence on the approach velocity V, which is also observed in similar experiments between a solid colloid probe and a liquid drop.[8] At low velocities, the force versus piezo displacement data are reversible. That is, the data are the same on approach and retract, with an approximately constant compliance region that has a slope that is much less than that for rigid−rigid surface contact because of drop deformation. At higher velocities that are comparable to velocities due to thermal motion of drops in a suspension, the force curves show hysteresis. Attractive forces of significant magnitude are observed when the drops are at the retract phase of the programmed velocity schedule. These results suggest the importance of the combined effects of electrical double layer repulsion between oil drops charged by adsorbed surfactant, hydrodynamic repulsion, and attraction arising from drainage of the aqueous film between the drops and drop deformation under the effects of surface forces, hydrodynamic forces, and surface tension.

The aim of this paper is to construct the simplest model that contains the above features to enable a quantitative assessment of their relative importance in determining the interaction between moving deformable drops.

2. Governing Equations

In previous studies of the interaction of a small rigid colloid probe and a large decane drop,[10] the interaction was observed to be independent of velocity within the range

* To whom correspondence should be addressed. E-mail: s.carnie@ms.unimelb.edu.au.

† Department of Mathematics and Statistics, The University of Melbourne.

‡ Department of Chemical and Biomolecular Engineering, The University of Melbourne.

(1) Mulvaney, P.; Perera, J. M.; Biggs, S.; Grieser, F.; Stevens, G. W. *J. Colloid Interface Sci.* **1996,** *183,* 614.

(2) Snyder, B. A.; Aston, D. E.; Berg, J. C. *Langmuir* **1997,** *13,* 590.

(3) Chan, D. Y. C.; Dagastine, R. R.; White, L. R. *J. Colloid Interface Sci.* **2001,** *236,* 141.

(4) Dagastine, R. R.; White, L. R. *J. Colloid Interface Sci.* **2002,** *247,* 310.

(5) Ducker, W. A.; Xu, Z.; Isrealachvili, J. N. *Langmuir* **1994,** *10,* 3279.

(6) Craig, V. S. J.; Neto, C.; Williams, D. R. M. *Phys. Rev. Lett.* **2001,** *87,* 054504.

(7) Bonnacurso, E.; Butt, H.-J.; Craig, V. S. J. *Phys. Rev. Lett.* **2003,** *90,* 144501.

(8) Aston, D. E.; Berg, J. C. *Ind. Eng. Chem. Res.* **2002,** *41,* 389.

(9) Dagastine, R. R.; Stevens, G. W.; Chan, D. Y. C.; Grieser, F. *J. Colloid Interface Sci.* **2004,** *273,* 339.

(10) Nespolo, S. A.; Chan, D. Y. C.; Grieser, F.; Hartley, P. G.; Stevens, G. W. *Langmuir* **2003,** *19,* 2124.

of the AFM. This allowed the result to be interpreted in terms of an equilibrium model. The force−stage position relationship $F(X)$ can be calculated from minimization of the total free energy of interaction, subject to a constant drop volume constraint.[3] In the present case, to account for the relative speed of approach of the drops, the hydrodynamics of the thin liquid film between the two drops must be incorporated into the model.

In the two decane drop AFM experiments, the drop radii are about 40 μm,[9] which set the upper length scale for the problem. The drops are moved by about 1 μm at a speed of the order of 1 μm/s, leading to an experimental time of around 1 s. By comparison, the drop deformation time is

$$\tau_{def} = \mu_D R_0 / \sigma$$

where μ_D is the drop viscosity, R_0 is the undeformed drop radius, and σ is the surface tension of the drops. The experiments are conducted in 8 mM sodium dodecyl sulfate (SDS) surfactant solution, which imparts a negative charge to the oil/water interface. The surface tension σ of the oil−water interface populated by adsorbed SDS is about 8 mN/m. These typical parameter values produce $\tau_{def} \approx$ 5 μs which is much less than the typical experimental time of around 1 s. Consequently, the deformation of the drop can be treated as a quasi-equilibrium phenomenon. For a similar argument in the context of the surface force apparatus, see ref 11.

The mean square velocity due to Brownian motion of a neutrally buoyant drop is related to thermal energy by

$$\langle V^2 \rangle = 3kT/m$$

For an oil drop of radius 40 μm at room temperature, this leads to a root-mean square velocity ≈ 7 μm/s. In the two decane drop AFM experiments velocities up to 13 μm/s are used.[9]

The major contribution to the force between the drops comes from a small interaction zone, of radial extent r_c, where the drops interact through a thin liquid film of thickness h. From geometry,

$$r_c^2 \approx R_0 h$$

and typically, in thin film drainage problems, $h \approx 0.1-1$ μm so we expect an interaction zone of width $r_c \approx 2-5$ μm. This separation of scales naturally divides the problem into an inner region that corresponds to the interaction zone with typical length scale r_c and an outer region that describes the drops as a whole with typical length scale of the undeformed drop radius R_0.

The other length scale in the problem is set by the range of any surface forces, here taken to be electrical double layer forces. At the salt concentrations used in the experiments, the Debye length is around 4 nm. Once the two drop surfaces approach to within $10-15$ Debye lengths, surface forces will begin to contribute to drop deformation.

Film thinning due to a radial drainage flow occurs in the inner region for which the usual lubrication approximations will hold and will lead to the standard thin film drainage equations first solved numerically in ref 12.

Because one drop is moving with velocity $\approx V$, there is hydrodynamic drag on the bulk of the drop. The ratio of hydrodynamic drag to surface tension forces can be estimated by the capillary number

$$Ca = \frac{\mu V}{\sigma}$$

which in these experiments is in the range $10^{-8}-10^{-6}$. Therefore, hydrodynamic drag can safely be ignored in the outer region and deformations of the drop in the outer region will be determined by (equilibrium) surface tension effects described by the Young−Laplace equation. This outer region is, thus, treated in the same way as previous equilibrium analyses of deformable interfaces.[3,13] However, unlike previous treatments, we find it necessary to account for the effects of the deformation produced in the outer region in a boundary condition for the interfacial velocity.

2.1. Film Drainage. A considerable amount of literature exists on modeling the drainage of a thin film between two drops. Two special cases have been studied in detail: drops interacting at constant force (appropriate for collisions driven by buoyancy forces)[14] or at constant (relative) velocity (modeling inertial collisions).[15] The former case has been studied in great depth as a singular perturbation problem that requires matching across inner and outer regions.[16] This has been generalized to drops of different sizes[17] and to include the effect of attractive surface forces that cause drop coalescence.[18]

The relative importance of hydrodynamics, surface forces, and deformation depends on the drop size. The thin film equations have been tested experimentally on drops of millimeter size[19,20] where dimpling of the thin film region typically occurs, with formation of a barrier ring that in turn restricts film drainage. In this regime, hydrodynamics is dominant, while repulsive surface forces determine the final film thickness at the barrier ring as well as the equilibrium film thickness.

For drops of micrometer size or smaller, the surface tension is so strong, that is, the capillary number so small, that under typical conditions the drops remain spherical and deformation can be neglected. However, in the intermediate size range of $10-100$ μm described here, hydrodynamics, surface forces, and deformation are all significant and must be included in the model.

One important modeling step is to decide whether tangential stresses are transmitted across the surfaces of the drops. If they are, which is generally the case for clean liquid−liquid interfaces, such surfaces are called *partially mobile*. The film velocity then has a slip velocity at the drop surface and the velocity field inside the drops must be accounted for in the governing equations. This model was carefully studied for nondeforming drops in ref 21 and with deformation in refs 14 and 16. In general, the film drainage then depends on the viscosity ratio of the drop and film.[22]

If the interface contains significant amounts of adsorbed surfactant, there is much evidence to suggest that the interface is *immobile* and no tangential stress is trans-

(11) Yang, S.-M.; Leal, L. G.; Kim, Y.-S. *J. Colloid Interface Sci.* **2002**, *250*, 457.

(12) Lin, C.-Y.; Slattery, J. C. *AIChE J.* **1982**, *28*, 147.

(13) Bardos, D. C. *Surf. Sci.* **2002**, *517*, 157.

(14) Yiantsios, S. G.; Davis, R. H. *J. Colloid Interface Sci.* **1991**, *144*, 412.

(15) Abid, S.; Chesters, A. K. *Int. J. Multiphase Flow* **1994**, *20*, 613.

(16) Yiantsios, S. G.; Davis, R. H. *J. Fluid Mech.* **1990**, *217*, 547.

(17) Rother, M. A.; Zinchenko, A. Z.; Davis, R. H. *J. Fluid Mech.* **1997**, *346*, 117.

(18) Saboni, A.; Gourdon, C.; Chesters, A. K. *J. Colloid Interface Sci.* **1995**, *175*, 27.

(19) Joye, J.-L.; Miller, C. A.; Hirasaki, G. J. *Langmuir* **1992**, *8*, 3083.

(20) Klaseboer, E.; Chevaillier, J. Ph.; Gourdon, C.; Masbernat, O. *J. Colloid Interface Sci.* **2000**, *229*, 274.

(21) Davis, R. H.; Schoenberg, J. A.; Rallison, J. M. *Phys. Fluids A* **1989**, *1*, 77.

(22) Bazhlekov, I. B.; Chesters, A. K.; van de Vosse, F. N. *Int. J. Multiphase Flow* **2000**, *26*, 445.

mitted into the drop.[10,20] This means that the film velocity at the drop surface is the same as that of the drop interface and a no-slip boundary condition applies. In this case, the thin film dynamics can be determined without the need to know the velocity inside the drops. Because the experimental system of interest here has adsorbed surfactant, we consider the drop surface to be immobile. Consequently, a no-slip boundary condition is applied at the drop surfaces and there is no need to consider velocity fields inside the drops.

While recent work has considered surfactant transport effects both between the bulk and the interface and within the interface due to Marangoni effects,[23,24] at surfactant concentrations at or above the critical micelle concentration, the oil/water interfaces will be populated by a close-packed surfactant layer. In this situation surfactant transport effects may be less important. In keeping with the objective to develop the simplest model to study the interplay of hydrodynamic interactions, drop deformation, surface forces, and approach velocities, we defer the consideration of surfactant transport effects to a future paper.

Under the above assumptions, together with axial symmetry and the usual thin lubricating film assumptions,[12] the governing equation in the inner region $r \approx r_c$ for the time evolution of the thickness of the liquid film between two liquid drops in the absence of surface forces is

$$\frac{\partial h}{\partial t} = \frac{1}{12\mu r} \frac{\partial}{\partial r}\left(r h^3 \frac{\partial p}{\partial r}\right) \quad (1)$$

where $h(r, t)$ is the film thickness as a function of radial coordinate r and time t, $p(r, t)$ is the excess hydrodynamic pressure in the film relative to the bulk liquid, and μ is the film viscosity (assumed Newtonian). This equation links the thinning rate of the film and the radial velocity due to a radial Poiseuille flow driven by a radial pressure gradient—see, for example, refs 12 and 20 for derivations.

In the inner region, the separation between undeformed surfaces, at an initial minimum separation h_0, is

$$h(r, 0) = h_0 + r^2/R_0 \quad (2)$$

where R_0 is the undeformed radius of the two identical drops.

We also need boundary conditions, suitable for constant approach velocity V. Due to axial symmetry, we have

$$\frac{\partial h}{\partial r} = 0 \quad \text{at} \quad r = 0 \quad (3)$$

$$\frac{\partial p}{\partial r} = 0 \quad \text{at} \quad r = 0 \quad (4)$$

and at large radial distances the surfaces are so far apart that the film pressure approaches the bulk pressure

$$p \to 0 \quad \text{as} \quad r \to \infty \quad (5)$$

2.2. Drop Shape. During the course of an experiment, the drop surfaces deform under the combined influence of hydrodynamic pressure $p(r, t)$ due to the drainage of the thin film between the drops and disjoining pressure $\Pi[h(r, t)]$ due to colloidal forces between the surfaces. From

(23) Blawzdziewicz, J.; Wajnryb, E.; Loewenberg, M. *J. Fluid Mech.* **1999**, *395*, 29.
(24) Yeo, L. Y.; Matar, O. K.; Perez de Ortiz, E. S.; Hewitt, G. F. *J. Colloid Interface Sci.* **2003**, *257*, 93.

the consideration of relative time scales of the approach between the drops and drop deformation time, we can treat drop deformations in a quasi-static manner whereby drop deformation can be described by the equilibrium Young−Laplace equation in the presence of equilibrium pressures $p(r, t)$ and $\Pi[h(r, t)]$.

The derivation of the Young−Laplace equation follows from a minimization of the drop surface energy in the presence of external forces, subject to a constant volume (incompressibility) constraint. In a quasi-static treatment of hydrodynamic and disjoining pressures, the Young−Laplace equation for the surface shape $z(r, t)$ has the form[3,13]

$$\frac{\sigma}{r} \frac{\partial}{\partial r}\left\{\frac{r(\partial z/\partial r)}{[1 + (\partial z/\partial r)^2]^{1/2}}\right\} = p + \Pi - \frac{2\sigma}{R} \quad (6)$$

where $2\sigma/R$ is the Lagrange multiplier associated with the constant drop volume constraint with $R \approx R_0$.

The interaction between the drops is confined to within an interaction zone—the inner region—characterized by the radial scale $r \sim r_c = (h R_0)^{1/2}$. Within this zone, we have $\partial z/\partial r \ll 1$, so eq 6 may be approximated by

$$\frac{\sigma}{r} \frac{\partial}{\partial r}\left(r \frac{\partial z}{\partial r}\right) = p + \Pi - \frac{2\sigma}{R} \quad (7)$$

This equation can be integrated to give the limiting form valid in the outer limit $(r \gg r_c)$ of the interaction zone

$$z(r, t) = z_0(t) - \frac{r^2}{2R} - H + G \ln\left(\frac{r}{r_c}\right) \quad \text{for} \quad r \gg r_c \quad (8)$$

where $z_0(t) \equiv z(0, t)$ and

$$G(t) = \frac{1}{\sigma}\int_0^\infty r\{p(r, t) + \Pi[h(r, t)]\}\, dr \quad (9)$$

$$H(t) = \frac{1}{\sigma}\int_0^\infty r \ln(r/r_c)\{p(r, t) + \Pi[h(r, t)]\}\, dr \quad (10)$$

The integrands for $H(t)$ and $G(t)$ are only nonzero within the interaction zone $r \sim r_c$ and vanish rapidly when $r \gg r_c$. The integral $G(t)$ is related to the force F between the two drops by

$$F = 2\pi\sigma G \quad (11)$$

In the present small deformation treatment, we seek solutions expanded in G/R_0. In the AFM measurement, the magnitude of G is of the order of 40 nm, so $G/R_0 \sim 10^{-3}$ is a genuinely small parameter.

If we assume for the time being that the cantilever does not deflect as the two identical drops approach each other, we have the following geometric relation between the drop profile $z(r, t)$, the film thickness $h(r, t)$, and displacement of the piezo stage $X(t) = \pm Vt$
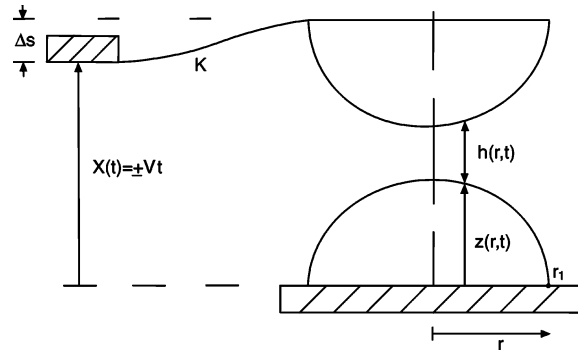
$$h(r, t) = X(t) - 2z(r, t) \quad (12)$$

thus, eq 7 can be written as

$$p + \Pi = \frac{2\sigma}{R_0} - \frac{\sigma}{2r} \frac{\partial}{\partial r}\left(r \frac{\partial h}{\partial r}\right) \quad (13)$$

Once a form for the disjoining pressure $\Pi(h)$ is specified, eqs 1 and 13 are to be solved numerically in the inner region until the solution matches the outer asymptotic form given by eqs 8 and 12. This will then give the functional form of the film thickness and the drop profiles.

Figure 1. Schematic diagram of the AFM geometry of two interacting drops. X measures the distance between the piezo stage and some fixed platform, Δs is the cantilever deflection, $z(r, t)$ is the drop height, and $h(r, t)$ is the film thickness.

Note that in eq 13 the deformed radius R has been replaced by the undeformed drop radius R_0. Making this replacement in the thin film equations produces a negligibly small $O(Ca^{1/2})$ correction to the boundary condition.

2.3. Matching the Inner and Outer Regions. In the numerical solution of the thin film equations, an asymptotic condition for the time derivative $\dot{h}(r, t)$ for $r \gg r_c$ is required. This can be obtained by differentiating eq 12 to give

$$\dot{h}(r, t) = \pm V - 2\dot{z}(r, t) \tag{14}$$

We will apply eq 14 at the outer part of the inner region at some large distance $r_{\max}$ on the inner scale, where eq 8 would be valid:

$$\dot{h}_{r\max} = \pm V - 2\dot{z}_{r\max} =$$
$$\pm V - 2\left[\dot{z}_0 - \dot{H} + \dot{G}\frac{1}{2}\ln\left(\frac{r_{\max}^2}{r_c^2}\right)\right] \tag{15}$$

To find $\dot{z}_0 - \dot{H}$, we have to match with the outer region.

In the outer region, the Young–Laplace equation can be written in the same cylindrical coordinates (z, r), solved in terms of elliptic integrals and expanded for small r to give (see eq 36 of ref 13)

$$z(r) = R\left[1 - \frac{r^2}{2R^2} \pm \sqrt{1 - \frac{r_1^2}{R_+^2}}\right] +$$
$$G\left[1 \pm \sqrt{1 - \frac{r_1^2}{R_+^2}} + \frac{1}{2}\ln\left(\frac{r^2}{4R^2}\right) \pm\right.$$
$$\left.\frac{1}{2}\ln\left\{\frac{1 + [1 - \{r_1^2/R_+^2\}]^{1/2}}{1 - [1 - (r_1^2/R_+^2)]^{1/2}}\right\}\right]$$

upper (lower)

where r_1 is the radial extent of the drop where it touches the solid base, R_+ is the maximum radial width of the drop, and the $+(-)$ sign refers to drops with an acute (obtuse) contact angle at the base (see Figure 1).

Now we take a small deformation expansion, using eqs 39 and 40 of ref 13, together with the definitions

$$R = R_0 + \delta R; \quad R_+ = R_0 + \delta R + G; \quad S \equiv \sqrt{1 - \frac{r_1^2}{R_0^2}}$$

to get

$$z(r) = -\frac{r^2}{2R} + R_0[1 \pm S] + \delta R\left[1 \pm \frac{1}{S}\right] +$$
$$G\left[1 \pm \frac{1}{S} + \frac{1}{2}\ln\left(\frac{r^2}{4R_0^2}\right) \pm \frac{1}{2}\ln\left(\frac{1+S}{1-S}\right)\right] \tag{16}$$

By comparing eq 16 with eq 8, we see that the terms in r^2 and $\ln r$ match, while equating the constants gives

$$z_0 - H = R_0[1 \pm S] + \delta R\left[1 \pm \frac{1}{S}\right] + G\frac{1}{2}\ln\left(\frac{r_c^2}{4R_0^2}\right) +$$
$$G\left[1 \pm \frac{1}{S} \pm \frac{1}{2}\ln\left(\frac{1+S}{1-S}\right)\right] \tag{17}$$

At this stage, we must specify the behavior of the three-phase contact line at the base of each drop. In ref 3, the contact line was considered pinned at some fixed radial position r_1 during interaction. In ref 13, the contact line was also allowed to slip while keeping a constant contact angle θ_p.

Considering the pinned case (constant r_1) first, we differentiate eq 16 with respect to time to get

$$\dot{z}_{r\max} = \delta\dot{R}\left[1 \pm \frac{1}{S}\right] + \dot{G}\frac{1}{2}\ln\left(\frac{r_{\max}^2}{4R_0^2}\right) +$$
$$\dot{G}\left[1 \pm \frac{1}{S} \pm \frac{1}{2}\ln\left(\frac{1+S}{1-S}\right)\right] \tag{18}$$

where we have evaluated the result at some suitably large value of $r = r_c = r_{\max}$.

At constant r_1, the change in mean curvature δR and force G are related by (eq 6 of ref 13)

$$\delta R = -G\frac{1}{1 - \cos\theta} \tag{19}$$

where θ is the contact angle of the *undeformed drop* at the piezo stage. We can then simplify eq 18 by using the geometric result (eq 45 of ref 13)

$$\sqrt{1 - \frac{r_1^2}{R_0^2}} = S = \pm\cos\theta \tag{20}$$

to give

$$\dot{z}_{r\max} = \dot{G}\left[1 + \frac{1}{2}\ln\left(\frac{r_{\max}^2}{4R_0^2}\right) + \frac{1}{2}\ln\left(\frac{1+\cos\theta}{1-\cos\theta}\right)\right] \tag{21}$$

which from eq 14 provides the required boundary condition for $\dot{h}$ for the pinned contact line case:

$$\dot{h}_{r\max} + \dot{G}\left[2 + \ln\left(\frac{r_{\max}^2}{4R_0^2}\right) + \ln\left(\frac{1+\cos\theta}{1-\cos\theta}\right)\right] = \pm V \tag{22}$$

For the case of constant angle $\theta = \theta_p$, we use the relation (eq 50 of ref 13)

$$\pm \sqrt{1 - \frac{r_1^2}{R_0^2}} = \cos\theta_p \left[1 - \frac{\delta R}{R_0}\tan^2\theta_p - \frac{G}{R_0\cos^2\theta_p} + O(G/R_0)^2 \right] \quad (23)$$

and the connection between deformation and force (eq 9 of ref 13)

$$\delta R = -G\frac{1}{(2 + \cos\theta_p)(1 - \cos\theta_p)} \quad (24)$$

to get

$$\dot{h}_{r\max} + \dot{G}\left[2 + \ln\left(\frac{r_{\max}^2}{4R_0^2}\right) + \ln\left(\frac{1 + \cos\theta_p}{1 - \cos\theta_p}\right) - \frac{2}{2 + \cos\theta_p} \right] = \pm V \quad (25)$$

Equation 22 or 25 is the requisite large r boundary conditions for the numerical solution of the inner film drainage equation if the cantilever does not deflect.

2.4. Incorporating the Cantilever Motion. The results in the preceding section have been derived on the assumption that the cantilever does not deflect. In fact as the bottom drop approaches the top drop, repulsive interaction will cause the cantilever to deflect which in turn increases the separation between the drops. This coupled motion of the cantilever and the drops must be incorporated into the formulation.

We model the cantilever as a plane attached to a fixed platform by a spring of stiffness K (see Figure 1). Then eq 12 will be replaced by

$$h(r, t) = X - 2z(r, t) + \Delta s \quad (26)$$

where Δs is the *deflection* of the cantilever. Assuming the cantilever behaves as a linear spring with spring constant K, Δs is related to the force F by

$$\Delta s = F/K = 2\pi\sigma G/K \quad (27)$$

where we use the convention that a positive force produces a positive (upward) deflection of the spring. Differentiating eq 26, we have

$$\dot{h}(r, t) = \pm V - 2\dot{z}(r, t) + 2\pi\sigma\dot{G}/K \quad (28)$$

which shows that the motion of the cantilever can be included through an extra term in the asymptotic boundary conditions, which in final form are

$$\dot{h}_{r\max} + \dot{G}\left[2 + \ln\left(\frac{r_{\max}^2}{4R_0^2}\right) + \ln\left(\frac{1 + \cos\theta}{1 - \cos\theta}\right) - \frac{2\pi\sigma}{K} \right] = \pm V \quad (29)$$

for the pinned contact line case and

$$\dot{h}_{r\max} + \dot{G}\left[2 + \ln\left(\frac{r_{\max}^2}{4R_0^2}\right) + \ln\left(\frac{1 + \cos\theta_p}{1 - \cos\theta_p}\right) - \frac{2}{2 + \cos\theta_p} - \frac{2\pi\sigma}{K} \right] = \pm V \quad (30)$$

for the constant contact angle case. These boundary

Table 1. Various Parameters Required To Describe Drop–Drop Interactions in an AFM

type	physical parameter	value
surface force	drop surface potential, ψ_0	-50 mV
	electrolyte concentration, n	8 mM
fluid	viscosity (water), μ	0.89 mPa·s
	drop surface tension, σ	8 mN/m
	undeformed drop radius, R_0	40 μm
	drop contact angle, θ	45–120°
AFM	cantilever spring constant, K	28 mN/m
	maximum piezo travel, $\Delta X_{\max}$	0.9 μm
	piezo drive velocity, V	0.1–13 μm/s
	initial separation, h_0	0.7 μm

conditions are needed to completely determine the numerical solution of the thin film drainage equations.

The two boundary conditions in eqs 29 and 30 have the following physical interpretation. If the coefficient of $\dot{G}$ is negative, then on approach, when $\dot{G}$ is positive, the separation will decrease at a slower rate than the drive velocity V, and on withdrawal, when $\dot{G}$ is negative, the separation will increase at a slower rate than the drive velocity V. In considering the sign of the coefficient of $\dot{G}$ in eq 29 or 30, we observe that the contribution due to deflections of the cantilever is always negative. This is because cantilever deflection will allow the top drop to back away as the bottom drop approaches and to follow the bottom drop as the latter withdraws. The extra term in eq 30 is always negative, because this reflects the extra degree of freedom in the system which allows the drops to slip at the contact line rather than bulge. The logarithmic term can be of either sign and vanishes for hemispherical drops ($\theta = \pi/2$). The dominant factors that are proportional to $\dot{G}$ are the first two terms

$$2 + \ln\left(\frac{r_{\max}^2}{4R_0^2}\right)$$

which are negative provided $r_{\max} < 2e^{-1}R_0$, which is always valid for sensible choices of $r_{\max}$. For typical values of $r_{\max}$, these two terms have a combined numerical value between -3 and -4. Thus, the dominant contributions come from the singular logarithmic terms which describe how the drop deforms under the increasing load G and thereby increases the separation on approach over what would be expected otherwise. In the appendix, we demonstrate the importance of the correct boundary conditions derived here in providing accurate numerical results.

3. Force between Drops in an AFM

The force between the drops can now be obtained by solving eqs 1 and 13 with the initial condition eq 2 and boundary conditions eqs 3–5 with either eq 29 or eq 30. Details of the method of numerical solution are described in the appendix.

Let us review the various parameters that describe the experiment. In this paper, we concentrate on understanding the interplay between hydrodynamics, drop deformation, and surface forces that produce the observed force curves. To this end, we will keep some parameters that specify the particular experimental system fixed but vary others where this helps to isolate the dominant influence of surface forces. A list of system parameters is given in Table 1.

3.1. Parameter Values. In the experiments of ref 9, a layer of adsorbed negatively charged surfactant on the drops produces a repulsive double layer disjoining pressure of the form

$$\Pi(h) = w \exp[-\kappa h(r, t)] \qquad (31)$$

where $w = 64nkT \tanh^2(e\psi_0/4kT) > 0$ depends on the surface potential ψ_0 on the drops and $\kappa = (2ne^2/\epsilon kT)^{1/2}$ is the usual Debye–Hückel parameter that depends on the salt concentration n. As we shall see, the superposition approximation in eq 31 for the electrical double layer interaction is sufficiently accurate for the typical range of distances of closest approach between the charged drop surfaces.

The surface potential ψ_0 is a property of the charged adsorbed species, the solution pH, and possibly the salt concentration n. Here we use a typical value for such charged interfaces.

For the salt concentration, we use the experimental value of 8 mM set by the critical micelle concentration of SDS. This in turn determines the range of the double layer forces, through κ^{-1}. Experiments can be done with different SDS concentrations which not only affects the Debye paramater κ but also the surface tension σ. Here we keep σ fixed at 8 mN/m, the measured value for the decane–SDS solution interface at 8 mM. The viscosity is kept fixed at the value of water (0.89 mPa·s).

In ref 9, two drops of radius 35 and 50 μm were used. Here we simplify the equations slightly by considering two equal drops of radius 40 μm. The contact angles on the piezo stage and the cantilever are unknown, but values in the range 45–120° would seem to cover the reasonable range. The special case of hemispherical drops ($\theta = 90°$ or $\theta_p = 90°$) is particularly simple.

The remaining parameters are characteristic of an AFM experiment. The cantilever spring constant K can be measured for a particular cantilever in various ways. Here we use the value given in recent experiments.[9]

The piezo stage is moved over a known distance ΔX_{max} of about 1 μm.[9] Similarly, the velocity V of approach/retract is easily varied from run to run. Values of V in ref 9 are in the range 0.16–13.2 μm/s (the reported values of V in ref 9 were too low by a factor of 2). As mentioned earlier this encompasses the range of Brownian velocities for particles of this size.

The calculation requires as input an initial separation h_0 between the drops. This is not known a priori in AFM experiments on deformable particles. A highly desirable outcome would be the use of computed force curves to determine the initial separation for a series of AFM runs.

The choices of other computational parameters are explained in the appendix.

3.2. Computed Quantities. Direct comparison with experiment can be carried out through $F(\Delta X)$ curves, for both the approach and the retract branches, for various choices of V, ΔX_{max}, and h_0. We show the ratio F/R_0 because, for equilibrium surface forces, the ratio F/R_0 between curved surfaces is proportional to the interaction energy per unit area between flat surfaces.[25] However, the same is not necessarily true for hydrodynamic interactions. It is also instructive to plot the force (or F/R_0), the central separation $h(0, t)$, and the velocity of the drop surface as functions of the time course of the experiment. Finally, the force F versus central separation $h(0, t)$ will be useful for visualizing the interaction between the two drops.

4. Results and Discussion

To illustrate the main features and capabilities of our model of the AFM experiment, we present results in the parameter range of the preliminary measurements of

(25) Hunter, R. J. *Foundations of Colloid Science*; Clarendon Press: Oxford, 1986; Vol. 1.
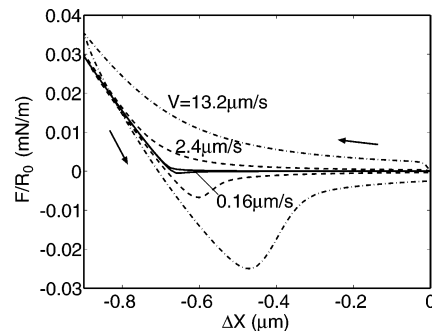
Figure 2. Force between two drops according to our model. The upper curves are on approach; the lower curves are on withdrawal. Approach speeds are 0.16 (solid), 2.4 (broken), and 13.2 (dashed–dotted) μm/s. Compare this figure to Figure 3 of ref 9.

Dagastine et al.[9] as summarized in Table 1. Our model provides insight into the dynamical behavior of the drop surface during interaction and can also quantify the interplay between surface forces, hydrodynamic interactions, and surface deformations during drop–drop interaction. Specifically, the two drops are positioned initially at the distance of closest approach of $h_0 = 0.7$ μm. The piezo displacement schedule is a single triangular sweep in which the surfaces are driven together at velocity V between 0.16 and 13.2 μm/s for $\Delta X_{max} = 0.9$ μm before the velocity is reversed. The three-phase contact line at the base of the drop is assumed to be fixed at r_1 and the unperturbed contact angle $\theta = 90°$.

In Figure 2 we show the force scaled by the undistorted drop radius (F/R_0) as a function of the piezo stage displacement ΔX at low, intermediate, and high speeds of approach and retract. At the lowest speed (0.16 μm/s) the approach and retract traces coincide and there is an apparent constant compliance region. On closer investigation, the slope of the apparent constant compliance region actually varies significantly with the maximum piezo displacement ΔX_{max}. Therefore, it is quantitatively incorrect to characterize the behavior of a deforming drop by an effective spring constant.[15]

At the intermediate speed (2.4 μm/s), the force is more repulsive along the approach trace and a small attractive force minimum can be observed in the retract trace. At high speed (13.2 μm/s), the force is even more repulsive along the approach trace and a strong attractive minimum is observed in the retract trace. The depth of this minimum is about half of the repulsive maximum at closest approach.

A convenient way to visualize the behavior of the system is to plot both F/R_0 and the distance of closest approach $h(0, t)$ between the two drops as a function of time as has been done in Figure 3. It is evident that a low speed 0.16 μm/s (Figure 3a) $h(0, t)$ tracks the piezo stage displacement initially until the undeformed drops are about to come into contact (point labeled A). Then $h(0, t)$ stops decreasing relatively abruptly at $h(0, t) = h_{min} \sim 0.026$ μm between $t \sim 4$–7 s. During this time interval the force F/R_0 increases and then decreases almost linearly with time. Salient points along the force curve are labeled A–D, and the corresponding drop profiles and pressure profiles are given as a function of radial position in Figure 4.

Turning first to the drop profiles (Figure 4a), we see that there is significant flattening of the drop surfaces at points B and C. At the point of maximum force, point B, the radial extent of the flattened regions is ~ 1 μm or about 5% of the undistorted radius. Outside this flattened region, for instance at points A and D, the drop profile is very close to parabolic. At low velocities, the general behavior
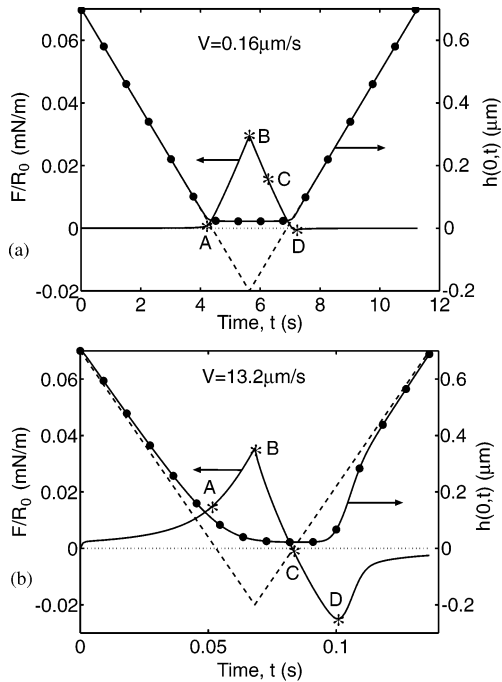
Figure 3. Force (solid curve), piezo stage position (broken curve), and central film thickness (●) as a function of time, on approach and withdrawal. Approach speeds are (a) 0.16 and (b) 13.2 μm/s.

of the drop surface during interaction is clear: the drops approach each other as almost undeformed surfaces until the separation h_{min} when disjoining pressure due to surface forces $\Pi(h_{min})$ is equal to the Laplace pressure $2\sigma/R_0$. The distance of closest approach then remains approximately constant, and the drop surfaces flatten to increase the effective area of interaction. It is this flattened area of interaction that contributes to the observed repulsive force.

Thus, force measurements in this regime sample colloidal forces at relatively large separations (see Figure 7).

The total pressure profile as well as the separate contributions to the pressure from electrical double layer and hydrodynamic interactions is detailed in Figure 4b–d. In this low velocity case, the pressure is due almost entirely to surface forces that arise from electrical double layer interactions and this is in accord with that observation that there is little hysteresis in the approach and retract traces. The hydrodynamic pressure profile has a larger range in the radial direction than the disjoining pressure profile, but the magnitude is smaller by a factor of 100. Also the magnitudes of the hydrodynamic pressures at points B and C are smaller than those at points A and D (Figure 4d) because the velocities of the drop surfaces at B and C are lower.

At high speed (13.2 μm/s) as shown in Figure 3b, the drop separation $h(0, t)$ no longer tracks the displacement of the piezo stage closely. At the point labeled A when the undeformed drops are about to come into contact, the repulsive force is almost 40% of the maximum value. There is also considerable asymmetry in the function $h(0, t)$ about the point of velocity reversal. However, between the force maximum (point B) and minimum (point D), $h(0, t)$ is nearly constant with a value of around 0.026 μm which is very close to that in the low speed result. At the force maximum, point B, the values of $h(0, t)$ at low (0.16 μm/s) and high (13.2 μm/s) speeds are similar and the radial extent of flattening of the drop surface is also comparable between the two cases; see Figures 4a and 5a.

For the high-speed case, the relative contributions of electrical double layer forces and hydrodynamic effects to the pressure profile vary at different times during the interaction. At point B, the hydrodynamic contribution is dominant, while at point C, where the net force is 0, the shorter-ranged (in radial extent) repulsive contribution to the pressure profile from surface forces is balanced by the attractive contribution from hydrodynamic interac-
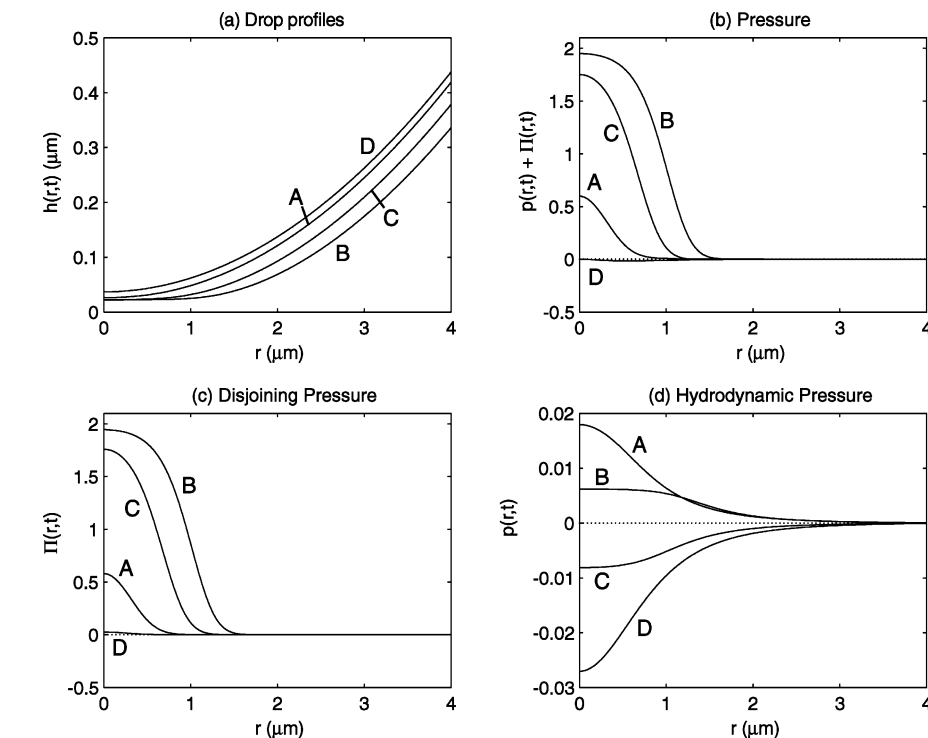
Figure 4. Film profiles (top left), film pressure profiles (top right), disjoining pressure profiles (bottom left), and hydrodynamic pressure profiles (bottom right) at four selected stages of approach followed by withdrawal. Pressure values are scaled by σ/R_0. Approach speed is 0.16 μm/s.
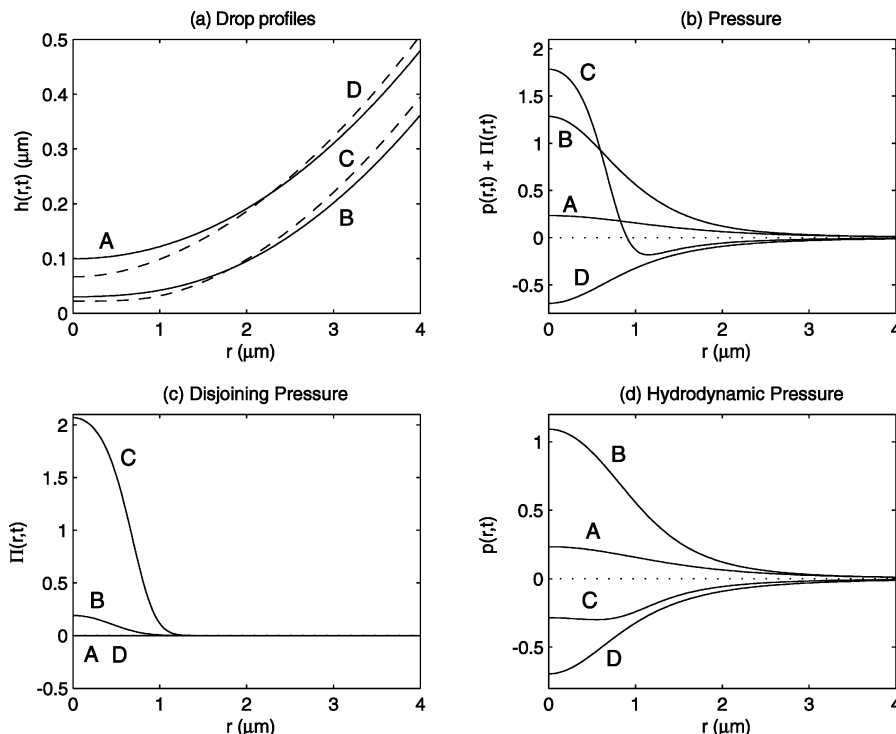
Figure 5. Film profiles (top left), film pressure profiles (top right), disjoining pressure profiles (bottom left), and hydrodynamic pressure profiles (bottom right) at four selected stages of approach followed by withdrawal. Approach speed is 13.2 μm/s.
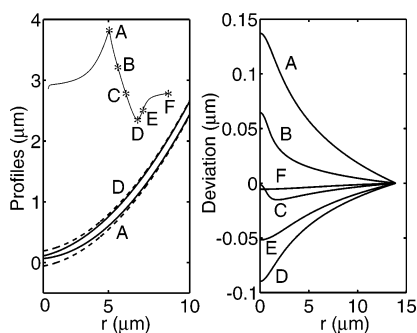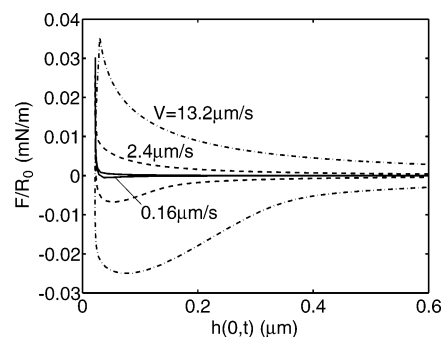

Figure 6. Profiles (solid) with parabolic approximation (dashed; left) and deviation of the profiles compared to a parabolic approximation (right) for $V = 13.2$ μm/s.

Figure 7. Force between two drops as a function of closest approach $h(0, t)$. Approach speeds are 0.16 (solid), 2.4 (broken), and 13.2 (dashed−dotted) μm/s.

tions which has a smaller magnitude but a longer range (r^{-4} decay in the radial extent).

Also, at point C the portion of the interface for which $r < \sim 1$ μm is closer together than that at the force maximum (point B). However, the portion of the interface for which $r > \sim 2$ μm is further apart at point C than at point B. This implies that during the initial part of the retract phase the velocity of the drop interface must change sign along the interface; see results in Figure 8 for details.

At point D, where the force between the drops is at the attractive minimum, the drop surfaces are at a separation (~ 0.1 μm) where surface forces are negligible compared to the hydrodynamic attraction (Figure 5c,d). It is interesting to observe that the drop surfaces at point D are pulled toward each other in the region around the point of closest approach ($r < \sim 2$ μm) by the attractive hydrodynamic interaction while the drop profiles at larger r (>2 μm) are similar to that at point A (Figure 5a).

In Figure 6, we quantify the deviations of the drop surface from an apparent parabolic profile along the retract branch, at a velocity of 13.2 μm/s. It is clear that the magnitudes of the deformations are small compared to the drop size and are consistent with the small deformation treatment we have used in this model to separate the

inner and outer solutions. Between the force maximum (point A) and the force minimum (point D) the drop surfaces change from being in compression to being in extension.

In Figure 7, the results in Figure 2 are presented in terms of the force scaled by the drop radius (F/R_0) as a function of the distance of closest approach $h(0, t)$ for the three velocities considered. We see that the attractive hydrodynamic minima extend to larger separations as the speed increases. In all three cases, the force curves rise sharply at $h(0, t) = h_{min} \sim 0.026$ μm, the separation at which the disjoining pressure from surface forces is balanced by the Laplace pressure of the drop. Because the drop surfaces do not come closer than 0.026 μm, the use of the simple exponential superposition form for the double layer interaction and the omission of weak van der Waals attraction that exists in an oil/water system are justified.

Insight about the dynamics of deformation of the drop surfaces can also be obtained from this model. In Figure 8, we show the velocity profile of the drop surface at various points in the inner region of the drop surface along the approach and retract traces of the force curves at 13.2 μm/s.
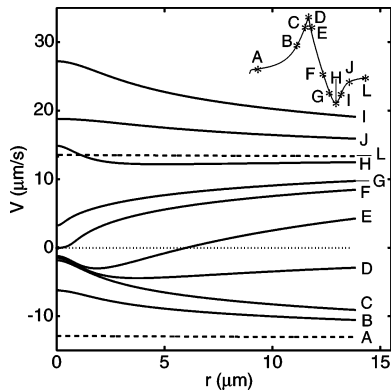
Figure 8. Velocity profiles of the drop surface along the approach and retract traces of the force curve for $V = 13.2 \, \mu$m/s.

(1) Along the approach branch, when the interaction between the drops becomes significant, the region of the drop surface near the point of closest approach ($r \sim 0$) becomes nearly stationary (curves C and D in Figure 8).

(2) During the early part of the retract trace, the central parts of the drop surfaces at small r are still approaching each other while the parts at large r are retracting (curve E in Figure 8). When the net force is 0 between the two drops (point F) the central portion of the drop surface remains almost stationary.

(3) However, at the force minimum (point H) the velocity of the surfaces near $r = 0$ begins to exceed, in magnitude, the retracting speed of the piezo stage. Indeed, shortly after the force minimum (point I) the entire inner part of the drop surface develops a velocity overshoot and retracts faster than the speed of the piezo stage.

(4) Eventually, the whole drop surface does attain the velocity of the piezo stage as expected (points J to L).

We should note that the observed velocity overshoot of the drop surface described above cannot occur without a proper matching of the inner solution of the drop profile to the outer solution that gave the proper boundary conditions for $\partial h/\partial t$ as given in eqs 29 or 30.

As we have remarked in the introduction, in the regime of drop sizes and velocities used in AFM experiments, surface tension forces are sufficiently strong (very small capillary number) to prevent the occurrence of a dimple in the drop surface during interaction. However, when the drop size in increased by 1−2 orders of magnitude, this model will predict dimpling due to hydrodynamic interactions.

If similar approach and retract calculations were carried out with a rigid surface (or infinite surface tension) where there is no deformation, the approach branch of the force curve would rise steeper and reach a higher magnitude. Upon the reversal of the piezo stage velocity, the retract branch of the force curve would be a mirror image of the approach branch about the $F = 0$ axis. Thus, as the surface tension of the drop decreases, the attractive minimum in the retract branch would be shallower and will be located nearer the point $\Delta X = 0$. Although the attractive minimum is due to hydrodynamic effects (see Figure 5d), the nature of the disjoining pressure Π can also affect the depth of this minimum in the range of drop sizes and velocity ranges we have studied. Within the current range of parameters, the distance of closest approach is controlled by the magnitude of the repulsive disjoining pressure. If this is reduced say by decreasing the Debye length, this will allow the two drop surfaces to come closer together on approach. On retraction, the hydrodynamic drainage flow associated with a thinner film will result in a deeper attractive minimum in the retraction branch of the force curve.

In this paper we have modeled the oil/water interface populated with surfactants simply as a deformable surface with a specified surface tension. Effects related to surfactant transport within the interface and between the interface and the bulk solution are omitted. Having obtained numerical results with our simple model we can return to examine the validity of omitting surfactant transport effects. We can estimate the magnitude of hydrodynamic shear forces at the oil/water interface in the thin drainage film (the inner region) as follows. In the lubrication approximation, the shear stress at the fluid interface τ_f is given by[20]

$$\tau_f = -\frac{h}{2}\frac{\partial p}{\partial r}$$

because v_r has the usual parabolic dependence on z. We can estimate the magnitude of the radial pressure gradient dp/dr from Figure 5d, for example, and taking $h \approx 30$ nm, which is the minimum thickness in the inner region (see Figure 7), we obtain a shear stress of the order $\tau_f \approx 2$ N m^{-2}, the same order of magnitude as found in ref 20 for much larger drops.

For an inner region of radius 1 μm the hydrodynamic shear stress exerts a shear force of around 6×10^{-12} N. This shear force is small compared to the interfacial tension force acting on the perimeter of the inner region which is estimated to be 5×10^{-8} N from an interfacial tension of 8 mN m^{-1}. Therefore, surfactant transport as a result of hydrodynamic shear is likely to be insignificant.

Alternatively, following ref 20 we can estimate the radial change in surface tension required to balance τ_f and immobilize the surface, leading to an estimate $\Delta\sigma/\sigma \approx 2 \times 10^{-4}$. Again, small changes in surface tension are sufficient to counteract the tangential stresses generated on approach.

Finally we observe that we employed the traditional stick boundary for the velocity field at the drop surface. We do not need to invoke the existence of a slip length or slip boundary condition that appears to be required to fit similar AFM measurements conducted between interacting solid surfaces. One possible explanation for this is that, at small separations, surface roughness that is present at solid surfaces renders the treatment of the film drainage by a lubrication approximation inappropriate and, therefore, a slip boundary condition has to be invoked as a heuristic correction. For fluid interfaces such surface roughness effects may not be an important issue.

More extensive AFM measurements of interacting drops are now available, and a detailed comparison of this theory with experimental data will be undertaken in a forthcoming publication.

5. Conclusions

We have developed a simple model for the force between drops mounted in an AFM that takes into account surface forces, hydrodynamics, drop deformation, and cantilever deflection; for the range of drop sizes 10 − 100 μm, these effects are equally significant. The development of a new boundary condition for the thinning equation, using matched asymptotic expansions, is the key feature that allows reliable numerical computation of the force between drops. This model already gives insight into the detailed dynamics of the deformation of the drop surface, such as the velocity overshoot, that are not readily evident in the AFM measurements.

The predicted force−displacement curves will allow detailed quantitative comparison with experiments that will be the subject of a forthcoming publication.

Appendix: Scaling and Numerical Solution

Before attempting a numerical solution, we first scale the governing equations using the scales suggested by Klaseboer et al.[20] The time scale is set by the approach velocity $t_c = h_c/V$, the Laplace pressure sets the pressure scale, the radial scale is set by the region of significant deformation $r_c^2 = R_0 h_c$, and h_c is chosen to nondimensionalize the equations. Different scales are typically used for approach at constant force.[14,18] With this choice, the various physical quantities are

$$h_c = R_0 Ca^{1/2}$$

$$r_c = R_0 Ca^{1/4}$$

$$p_c = \sigma/R_0$$

$$t_c = \mu Ca^{-1/2}/p_c$$

where $Ca = \mu V/\sigma$ is the capillary number—the ratio of viscous forces to surface tension forces.

Then the nondimensional forms of the equation become

$$\frac{\partial h}{\partial t} = \frac{1}{12r}\frac{\partial}{\partial r}\left(rh^3\frac{\partial p}{\partial r}\right) \tag{32}$$

$$p + \Pi = 2 - \frac{1}{2r}\frac{\partial}{\partial r}\left(r\frac{\partial h}{\partial r}\right) \tag{33}$$

$$G = \int_0^\infty r[p(r, t) + \Pi]\,dr \tag{34}$$

with initial and boundary conditions

$$h(r, 0) = h_0 + r^2 \tag{35}$$

$$\frac{\partial h}{\partial r} = 0 \quad \text{at} \quad r = 0 \tag{36}$$

$$\frac{\partial p}{\partial r} = 0 \quad \text{at} \quad r = 0 \tag{37}$$

$$p = 0 \quad \text{at} \quad r = r_{max} \tag{38}$$

$$\frac{\partial h}{\partial t} + \frac{\partial G}{\partial t}\mathscr{F} = \pm 1 \quad \text{at} \quad r = r_{max} \tag{39}$$
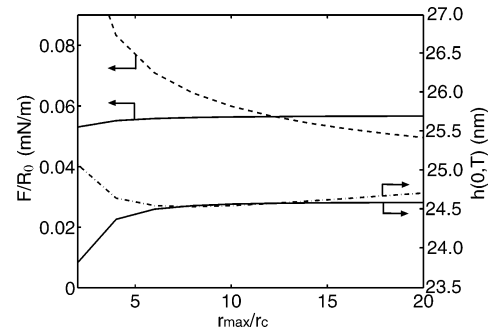
where

$$\mathscr{F} = 2 + \ln\left(\frac{r_{max}^2 Ca^{1/2}}{4}\right) + \ln\left(\frac{1 + \cos\theta}{1 - \cos\theta}\right) - \frac{2\pi\sigma}{K} \tag{40}$$

in the case in which the three-phase contact line of the drop is fixed at $r = r_1$ by eq 20). For the constant contact angle boundary condition $\theta = \theta_p$ (fixed)

$$\mathscr{F} = 2 + \ln\left(\frac{r_{max}^2 Ca^{1/2}}{4}\right) + \ln\left(\frac{1 + \cos\theta_p}{1 - \cos\theta_p}\right) - \frac{2\pi\sigma}{K} - \frac{2}{2 + \cos\theta_p} \tag{41}$$

A detailed numerical study of two large drops (radius $\sim 1500\,\mu$m) has been carried out by Klaseboer et al.[20]

Figure 9. Scaled force F/R_0 and central film thickness at the end of the 1 μm approach of two drops initially 0.7 μm apart, as a function of r_{max}, the size of the computational domain. The broken curves denote results using the simple boundary condition eq 43, and the solid curves are results obtained with the new boundary condition eq 39.

They considered film drainage and dimple formation at a film thickness of the order of 1 μm, where surface forces can be omitted. For the range of drop sizes considered in the present work (radius 40 μm), the drainage films have a thickness at which surface forces cannot be neglected.

Our new boundary condition eq 39, which involves the derivative of a functional of the dependent variable h, changes the mathematical nature of the problem—we no longer have a simple set of partial differential equations. However, on discretization in r as in the method of lines, we get a system of equations with a more standard form.

We use central differencing in r in eqs 32 and 33 to obtain a system of differential equations for $h_j(t) \equiv h(j\Delta r, t)$, $j = 0, ..., N$ where $N = r_{max}/\Delta r$. We use a uniform grid in $r = [0, r_{max}]$ with $\Delta r = 0.02$ and $r_{max} = 10$ which produces a system of 500 equations. The boundary conditions at $r = 0$ are used to produce the equation for $\dot{h}_0$, and eq 39 provides the equation for $\dot{h}_N$. The functional G is obtained by evaluating the following integral using Simpson's rule

$$G = \int_0^{r_{max}} r[p(r, t) + \Pi]\,dr$$

which relates G to all the other variables h_j as an algebraic constraint.

In summary, the final system of equations has the form

$$\begin{pmatrix} 1 & 0 & \cdots & 0 & 0 \\ 0 & 1 & 0 & \cdots & 0 \\ & & \vdots & & \\ 0 & 0 & \cdots & 1 & \mathscr{F} \\ 0 & 0 & \cdots & 0 & 0 \end{pmatrix} \begin{pmatrix} \dot{h}_0 \\ \dot{h}_1 \\ \vdots \\ \dot{h}_N \\ \dot{G} \end{pmatrix} = \begin{pmatrix} f_0 \\ f_1 \\ \vdots \\ \pm 1 \\ G - \sum_j w_j g(h_j) \end{pmatrix} \tag{42}$$

where $\mathscr{F}$ is the coefficient of $\dot{G}$ in eq 39 and f_j represent the discretized contributions of the thinning equation and normal stress balance.

This system has a singular mass matrix and is a differential-algebraic equation of index 1. It can be solved by standard software, in our case Matlab's ode15s.

In previous work, Klaseboer et al.[20] used the boundary condition for the thinning rate

$$\frac{\partial h}{\partial t} = \pm 1 \quad \text{at} \quad r_{max} \tag{43}$$

which neglects the deformation of the drop by the force G. In their work, they compared the film profile $h(r, t)$ and, in particular, the central film thickness $h(0, t)$ with experiments. We shall see that the central film thickness

is not sensitive to the thinning rate boundary condition, which explains why their results appeared reasonably independent of the choice of r_{max}. The force, which is of central interest in our problem, is sensitive to the thinning rate boundary condition.

To see why the new boundary condition is necessary in our calculations, consider the central film thickness $h(0, t)$ and force F calculated for different choices of r_{max}. To have confidence in the numerical results, the results need to be independent of r_{max} once it is large enough to be outside the interaction zone. In Figure 9, we show results for the central film thickness for a range of r_{max} values. The other parameters are that the initial central film

thickness (surface separation) is $0.7\,\mu$m, the piezo is driven in $1\,\mu$m at a velocity $V = 13.2\,\mu$m/s, the undeformed contact angle $\theta = \pi/3$, and the cantilever stiffness is $K = 28$ mN/m. Also shown are results using the simple boundary condition eq 43. For the film thickness, we see in Figure 9 that the choice of boundary condition is not crucial, although the new boundary condition does give results noticeably less dependent on r_{max}. By contrast, a similar plot for the force divided by R_0 shows that no sensible choice of r_{max} can be made using eq 43 but that the results are stable for $r_{max} \geq 6$ with our new boundary condition.